

Failure analysis of a hip implant by using the FITNET fitness for service procedure

S. Cicero *, F. Gutiérrez-Solana, J.A. Álvarez, L. Sánchez

Departamento de Ciencia e Ingeniería del Terreno y de los Materiales, E.T.S. de Ingenieros de Caminos, Canales y Puertos, Universidad de Cantabria, Avda. de Los Castros s/n, 39005 Santander, Spain

Received 23 February 2006; received in revised form 9 June 2006; accepted 23 June 2006
Available online 22 August 2006

Abstract

This paper analyses the failure of a hip implant, which occurred nine months after the corresponding surgery operation. The base material of the implant is a metallic matrix piece of alloy Ti–6Al–4V, coated by two surface layers; the first one is a 50 μm thick layer of pure porous titanium and the other one is a hidroxiapatite ceramic layer of 150 μm . The study uses scanning electron microscopy techniques and X-ray microanalysis in order to analyse the coatings and the state of the interphases, as well as the type of fracture present on the fracture surface. From this analysis, it is concluded that failure has been produced by a fatigue process initiated on imperfections and alumina inclusions (Al_2O_3) located in the interphase area between the base material and the titanium coating. An analysis has also been performed in order to justify the failure conditions and the life time of the implanted piece, based on the fracture mechanics approach of the FITNET structural integrity assessment procedure.

© 2006 Elsevier Ltd. All rights reserved.

Keywords: Hip implant; Titanium; Coating; Failure assessment diagram; Fatigue; FITNET

1. Introduction

Metals have been used successfully as biomaterials in the last decades. They are mainly used in the field of orthodontics and dental implants and for orthopaedic use in knee and hip implants. The most commonly used metals for structural applications in the human body are stainless steels, cobalt–chromium alloys and titanium and its alloys. After biocompatibility, the main requirements for these materials are that they must be resistant to degradation when inserted in the body and that they must have optimum mechanical properties [1–5].

Titanium biocompatibility is excellent. Implant devices made of titanium and its alloys show little or no reaction with the tissues surrounding the implant. Titanium corrosion resistance is provided by the stable oxide layer that appears on its surface which, when damaged, reconstitutes itself at body temperature. Although a wide range of titanium alloys have been developed for industrial applications, only alloy Ti–6Al–4V and four

* Corresponding author. Tel.: +34 942200917; fax: +34 942201818.
E-mail address: ciceros@unican.es (S. Cicero).

Nomenclature

a	crack length
D	diameter
E	modulus of elasticity
EDS	X-ray energy dispersive analysis technique
FAL	failure assessment line
FAD	failure assessment diagram
FFS	fitness-for-service
$f(L_T)$	plasticity correction function
g	parameter used in Eq. (14)
K_I	elastic stress intensity factor
K_{IC}	fracture toughness
K_T	ratio of stress intensity factor to the fracture toughness
L_T	ratio of externally applied load to the yield load
M	bending moment
N	number of cycles
N	estimated strain hardening exponent
P	externally applied load
P^*	externally applied load considering dynamic effects
P_L	yield load
R	radius
SEM	scanning electron microscopy
Y_F	geometric factor
ΔK	stress intensity factor range
ψ	parameter used in Eq. (14)
σ_B	bending stress
σ_C	compression stress
σ_T	total applied stress
σ_Y	yield stress
σ_u	ultimate tensile strength
μ	parameter used in Eq. (8)

grades of pure titanium are commonly used as implant material in human body applications. Among these, alloy Ti–6Al–4V offers the best combination of properties when used in implants with structural duties. It has much higher yield and ultimate strengths than pure titanium, as well as good ductility. It is generally produced by forging but can also be cast in order to obtain the required shape. Moreover, alloy Ti–6Al–4V can be strengthened by controlling the composition and adjusting different manufacturing parameters. The fatigue life of this alloy can be doubled [1] through the appropriate processing methods. As a consequence of the tough titanium oxide layer, the friction and wear behaviour of titanium alloys are better than most of the other metals. This layer remains intact under low loads and low sliding rates, which are characteristic of articulation movements in human bodies [1].

In the 1990s, despite the high biocompatibility of titanium, coatings of bioactive materials which are capable of inducing a biological response in the adjacent human tissues have come into widespread use [6–8]. These biomaterials are used to coat the metallic substrata of the implant after their application by means of plasma thermal spray, which makes it easy to obtain the appropriate thickness and porosity. One of these biomaterials is the hydroxiapatite (here HA), a phosphate of pentacalcium $\text{Ca}_5\text{OH}(\text{PO}_4)_3$ with a purity of over 98% and 10% of porosity. It has properties such as a Ca/P proportion of 1.67 and crystalline structure with interconnected macropores (150–200 μm) and micropores (3–5 μm) that make this material an identical compound to

the human trabecular bone [9,10]. After being implanted, the biomaterial presents a chemical reaction with the neighbouring bone, which induces the formation of trabeculae and its mineralization.

The aim of this paper is to determine the causes of the premature failure of a hip implant nine months after being implanted.

2. Reception and preparation of the sample

The sample, shown in Fig. 1, is a hip implant broken into two pieces. The section of the implant is circular and the diameter is 10 mm. It was extracted from the patient after its fracture. At reception, the sample was dirty with many blood traces. Also, remains of bone material were appreciated on the stem or lower part since the implant had begun to be integrated in the femur by osteointegration reactions. However, there is no presence of these bone traces in the upper part. It should be noted that the fracture surfaces, mainly the one on the lower part, were quite badly damaged due to the surgery extraction process, making the analysis more difficult.

The first step performed in the analysis was to make a cut in the piece with the least damaged fracture surface (upper part). After that, the obtained coupon was cleaned so that it could be observed through scanning electron microscopy (SEM). Also, the cut face of the coupon opposite the fracture surface was prepared by polishing in order to perform the analysis of the chemical composition of the base material and the different layers.

3. Experimental methodology

3.1. Introduction

The methodology started with the identification of the microstructure of the different materials using scanning electron microscopy (SEM) complemented by X-ray energy dispersive analysis techniques (EDS). This analysis was performed on the prepared, cleaned, polished surface of the coupon.

Afterwards, the fracture surface was observed by SEM in order to identify the fracture mechanisms and other possible previous cracking processes. The fractographical analysis was complemented by EDS analysis, which was performed in order to identify the microstructural elements associated with the fracture processes.

3.2. Base material and coatings characterization

Fig. 2 shows the structure of the coatings, base material and the corresponding interphases. It is important to notice the irregularity of the coatings and the discontinuities observed in the interphase between the base material and the titanium coating, as can be clearly seen in the micrographs of Fig. 3. The micrograph in Fig. 4, which is amplified by 3500 times, shows the apparently crystalline nature of the discontinuities. They will be designated as inclusions in the base material–titanium coating interphase.

The configuration shown (irregular layers of coating with inclusions in the interphase between the base material and the titanium coating) was also observed in all the other areas of the coupon's surface. Therefore, it is representative of the whole implant section. It was verified by running the SEM all over the perimeter of the polished section of the coupon.



Fig. 1. Aspect of the implant on reception.

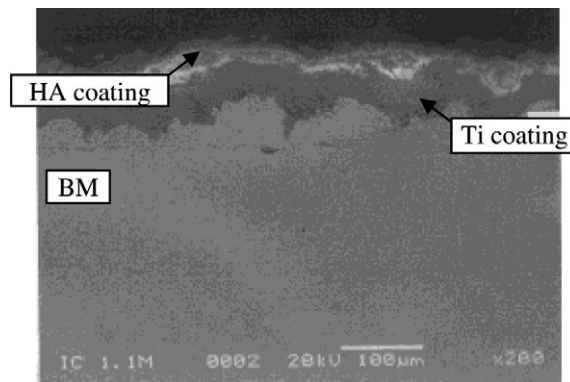


Fig. 2. General aspect of the coatings and the base material.

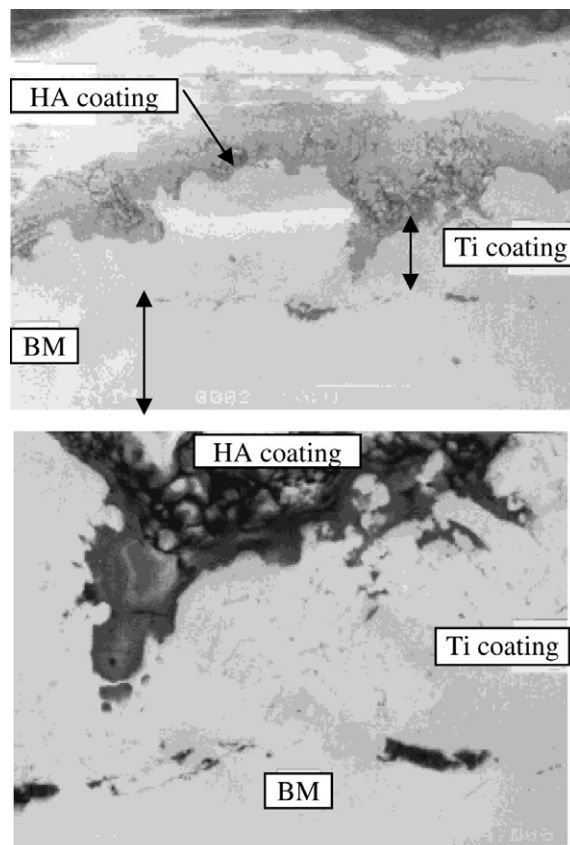


Fig. 3. Detailed image of the coatings: Ti coating varies between 10 and 100 μm . Inclusions in the interphase between base material and the titanium coating can be observed.

Table 1 shows the results of the EDS analyses. The most significant conclusion is that the base material is a Ti–Al–V alloy with bigger quantities of Al than expected for this type of alloy. Also, on the base material, there is a nearly pure titanium coating whose thickness varies between 10 and 100 μm and a HA coating with a calcium/phosphorous relation of near 1.4, slightly lower than the value of 1.67 predicted theoretically [9]. It is also worth noting the irregularity of the coatings and the discontinuities on the base material–Ti coating interphase, as shown in Fig. 3.

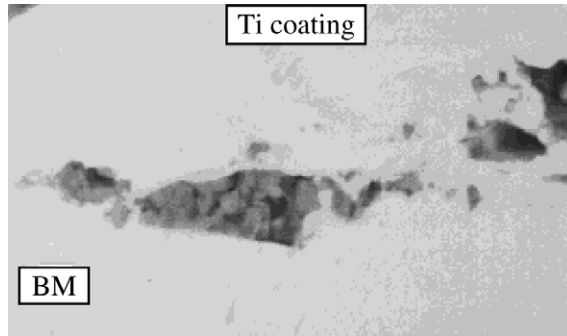


Fig. 4. Detailed image of the interphase between base material and the titanium coating, showing the clustering of alumina inclusions.

Table 1
Chemical composition (% in weight) of the base material and coatings

	Ti	Al	V
Base material	86.9	9.3	3.8
Ti coating	99.6	0.4	–
	P	Ca	Na
HA coating	39.5	55.9	2.3

The analysis performed on the inclusions observed in the interphase between the base material and the titanium coating confirms that there were crystals of alumina inclusions (Al_2O_3). These crystals, whose size is in the order of $1\ \mu m$, are clustered and generate relatively plane areas of discontinuity which are between 5 and $20\ \mu m$ long. The inclusions can be easily identified in the above mentioned interphase since they appear as dark areas in Figs. 2–4.

3.3. Fractographic analysis

A macroscopic observation of the fracture surface allowed the fatigue growth lines of the crack to be observed. It was determined that a crack generated by fatigue reached a maximum extension of 6.5 mm. Fig. 5 shows a scheme of the fracture surface and Fig. 6 shows in a SEM micrograph the growth lines of

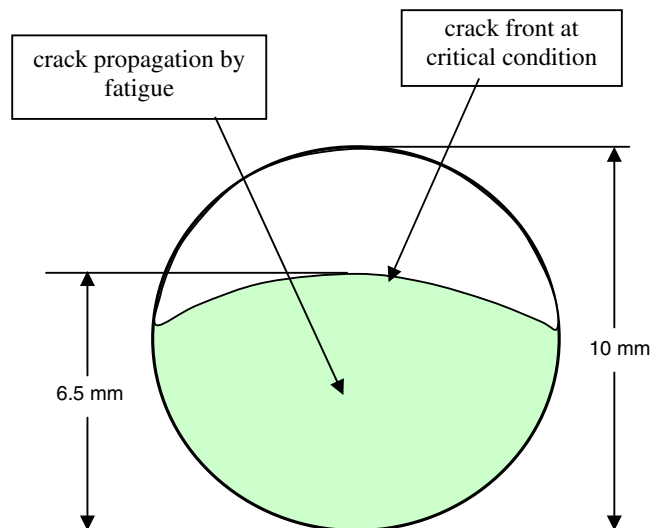


Fig. 5. Scheme of the crack geometry at failure.

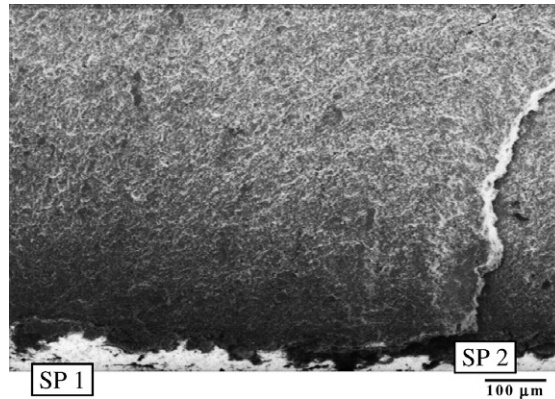


Fig. 6. Starting area of the fatigue growth with two marked starting points.

the crack, generated by fatigue, in the neighbouring area to two starting points (SP) located at both of the lower squares of the micrograph.

A series of steps were performed in the surface analysis. A complete SEM observation was made along the crack growth area from the theoretical starting point, observed macroscopically and close to the starting points shown in Fig. 6, to the crack front at failure. It was performed in order to validate the macroscopic observation. The micrographs shown in Fig. 7, taken at the fatigue crack growth zone, present a fatigue

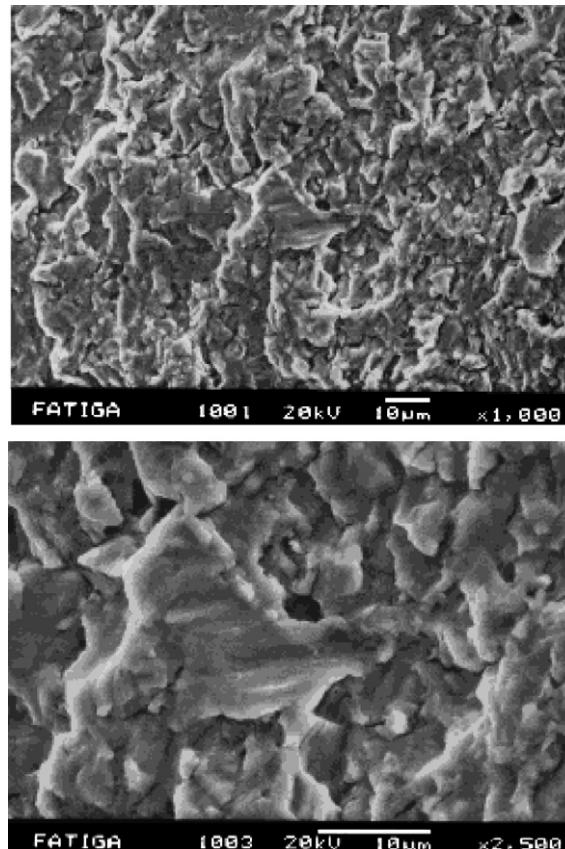


Fig. 7. Fatigue surface.

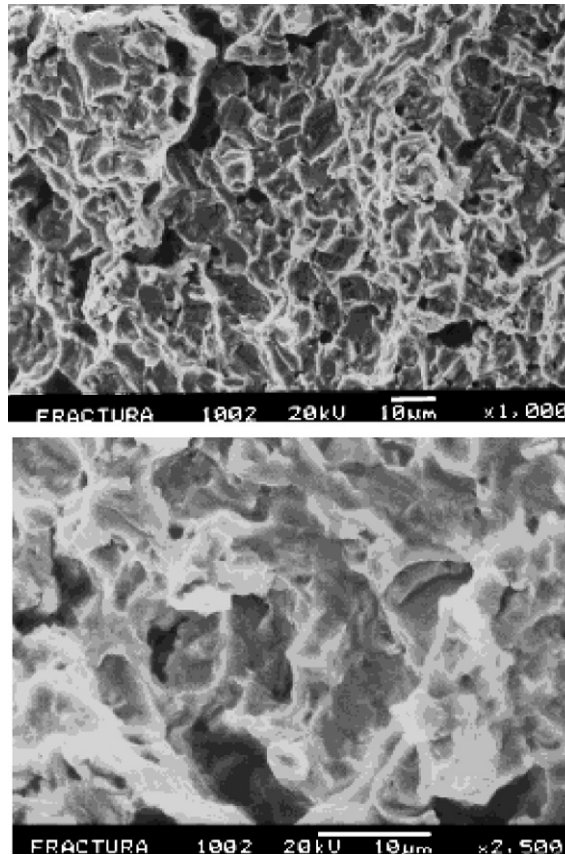


Fig. 8. Fracture surface.

surface which is characteristic of fatigue processes in these titanium alloys [11–14]. Fig. 8, taken at 8 mm from the starting point (outside the fatigue zone), shows formation and coalescence of microvoids, which is characteristic of plastic collapse mechanisms in these materials.

The micrographic observation of the initiation sites of the fatigue crack shows the existence of substantial disbanding, such as discontinuities in the interphase between the base material and the titanium coating. The micrograph in Fig. 9 shows that discontinuity, which is associated with the presence of a set of Al_2O_3 crystal clusters.

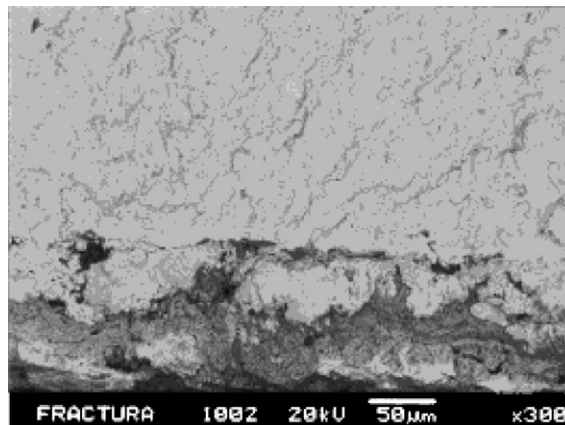


Fig. 9. Detailed image of the first starting point.

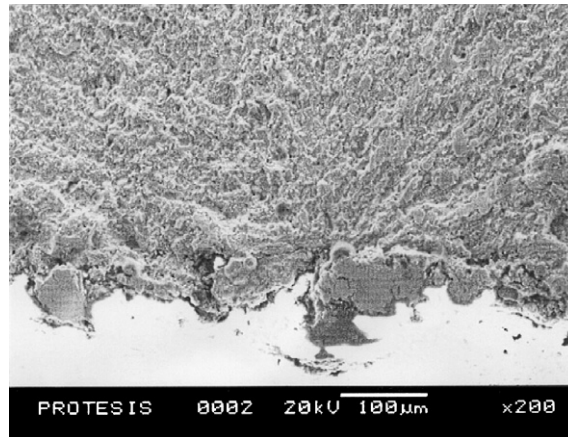


Fig. 10. Detailed image of the starting area.

In both observed starting points the greater the presence of Al_2O_3 crystal clusters, the thinner the titanium coating, establishing a local notch effect on them (see Fig. 10). Initially, two crack planes propagate independently from both initiation sites for approximately 2 mm. Then, the two planes of fracture join and generate one single crack front that, after growing, established the shape and size of the final crack observed at failure.

4. Analytical work

4.1. Introduction

After the previous analysis, a structural integrity assessment is performed following the steps, contents and formulation provided by the FITNET FSS procedure, which has recently been developed within the European thematic network FITNET [15], based on the previous SINTAP procedure [16].

4.2. Inputs

4.2.1. Flaw information

From microscopy analysis, it was determined that a crack grew from an initial defect originated in the irregular coating, as shown in Figs. 2 and 3. Fig. 10 shows another micrograph of the initiation area. The defect was around 0.1 mm deep at the initial stage (the size of the irregularities located in the interphase) and 6.5 mm deep at failure, as has been shown in Fig. 5. The crack front during the propagation process is not a straight crack front or a semicircular crack front, but rather its geometry is between these two for the whole process.

4.2.2. Stresses

Fig. 11 presents a schema of the working conditions of the implant at failure. The implant worked as a cantilever beam, with a non-centred load applied, transmitted at the contact implant-hip bone, due to the body weight of the patient. The assumption of cantilever beam fixed up to the fracture surface is supported by the absence of adhered bone to the upper part of the piece. The direction of the load is considered to be parallel to the bone so neither shear nor torsion stresses are considered. This hypothesis is very closed to the real situation and accurate enough for the purposes of this analysis. Therefore, a mixed stress state at the ligament is achieved due to bending and compression.

At the crack front, the obtained tension stresses are responsible for the final fracture:

$$\sigma_{T,\max} = \sigma_B - \sigma_C \quad (1)$$

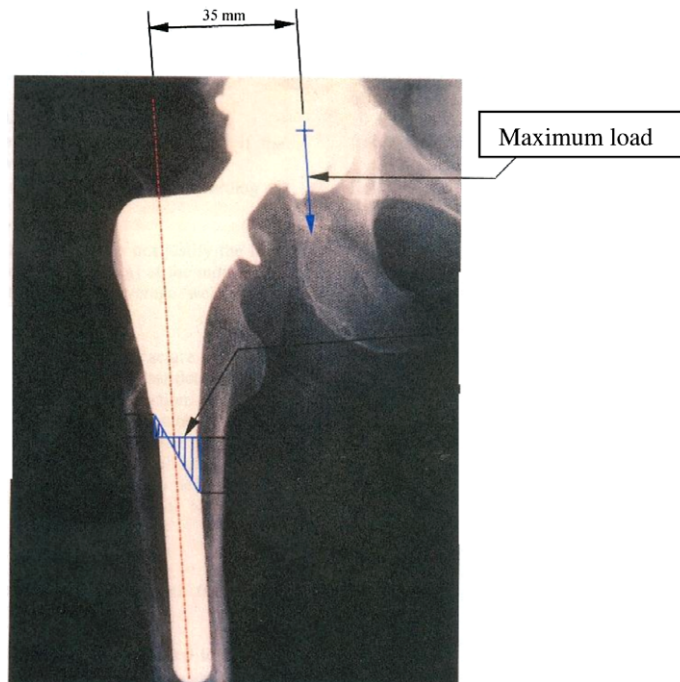


Fig. 11. Scheme of the working conditions.

where

$$\sigma_B = \frac{32 \cdot M}{\pi \cdot D^3} \quad (2)$$

$$\sigma_C = \frac{4 \cdot P^*}{\pi \cdot D^2} \quad (3)$$

Many studies have been performed (i.e., [17–22]) in order to know the peak forces that appear in hip implants when the patient is walking. From them, a value of 2.5 BW (body weight) seems to be reasonable. The shape of the loading cycles during the walking process can be found in [23–25], being the main conclusion that stresses reach the maximum value derived from the peak forces, remain some time at high values close to the maximum value and finally decrease to values close to zero.

During the whole process which starts with the surgery implant and finishes with the failure of the prosthesis, three stages can be distinguished:

- (1) Crack nucleation: here it is considered to be non-existent as defects have been detected in the fractographic analysis.
- (2) Quick crack propagation (stage 1): In this stage, the patient is considered to carry out a “normal” activity. It is assumed that he/she could walk 2 h per day with a pace of one step per second (0.5 cycles/s). Peak forces (P^*) are considered to be equal to 2.5 BW.
- (3) Slow crack propagation (stage 2): The crack has grown in the previous stage and the patient has started to feel pain due to the flexibility of the system. He/she reduced his/her activity (1 h/day) and started to use crutches. The dynamic effects were mainly cushioned by them and by the slower movements of the patient, so it is considered that peak forces are equal to 1.0 BW. This hypothesis is supported by the FAD analysis shown below, where considering that value, the actual weight of the patient is obtained as the critical load at failure.

4.2.3. Material properties

These are the data available for the base material [26]:

$$\begin{aligned}
 K_{IC} &= 110 \text{ MPa m}^{1/2} \\
 \sigma_Y &= 895 \text{ MPa} \\
 \sigma_u &= 1000 \text{ MPa} \\
 E &= 114 \text{ GPa} \\
 \frac{da}{dN} &= 3.54 \times 10^{-14} \cdot (\Delta K)^{4.19}
 \end{aligned} \tag{4}$$

when ΔK is given in $\text{MPa m}^{1/2}$ and da/dN in m/cycles .

Continuous yielding is assumed.

4.3. Assessment

4.3.1. Failure

The assessment of the fracture conditions has been performed following the FITNET procedure [15]. Options 0 (basic) and 1 (standard) have been chosen for the assessment as a consequence of the existing information about material properties:

Toughness, yield stress and ultimate tensile stress define the FAL (failure assessment line) as:

Option 0:

$$K_r = (1 + 0.5(L_r)^2)^{1/2} (0.3 + 0.7 \cdot \exp(-0.6L_r^6)) \quad \text{for } L_r \leq L_{r\max} \tag{5}$$

$$K_r = 0 \quad \text{for } L_r \geq L_{r\max} \tag{6}$$

$$L_{r\max} = 1 + (150/\sigma_Y)^{2.5} \tag{7}$$

Option 1:

$$K_r = (1 + 0.5(L_r)^2)^{1/2} (0.3 + 0.7 \cdot \exp(-\mu L_r^6)) \quad \text{for } L_r \leq 1 \tag{8}$$

$$\mu = \min[0.001 \cdot (E/\sigma_Y); 0.6] \tag{9}$$

$$K_r = K_r(1) \cdot L_r^{\frac{N-1}{2N}} \quad \text{for } 1 < L_r \leq L_{r\max} \tag{10}$$

$$N = 0.3(1 - \sigma_Y/\sigma_u) \tag{11}$$

$$L_{r\max} = 0.5(\sigma_Y + \sigma_u)/\sigma_Y \tag{12}$$

The FAL is defined in the $L_r(P/P_L) - K_r(K_I/K_{IC})$ field, determining the corresponding failure assessment diagram (FAD). P_L represents the limit load condition of the component due to plastic collapse.

As mentioned above, peak forces are considered to be 1.0 BW due to the effect of the crutches and the slower movements of the patient.

At failure conditions, the limit load solution has been taken considering the complete plastification of the residual ligament and establishing the equilibrium of loads and moments. The results for the two considered crack fronts have been these:

Straight crack front

$$P_L = 0.566 \text{ kN}$$

Semicircular crack

$$P_L = 0.895 \text{ kN}$$

They can also be obtained from the FITNET limit load annex [15].

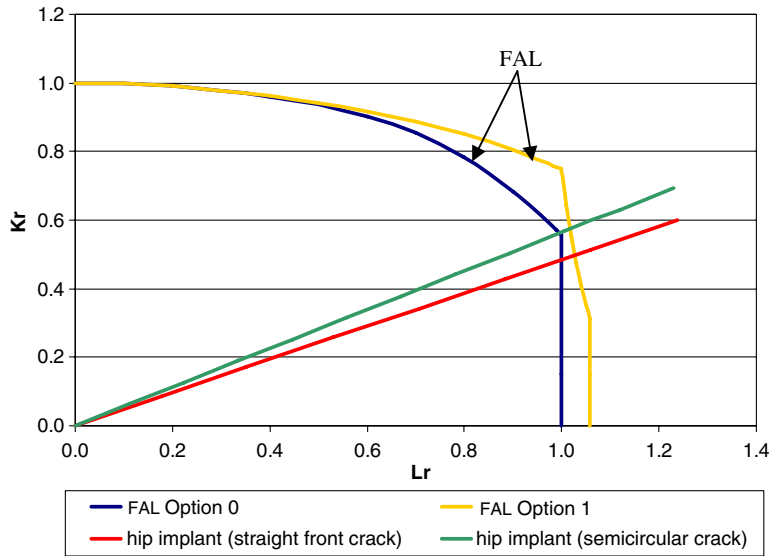


Fig. 12. Assessment of critical conditions by using FAD analysis.

The stress intensity factor, K_I , can be established as a function of the applied load, P , from the equation given below:

$$K_I = \sigma \cdot Y_F(a/D) \cdot (\pi a)^{1/2} \tag{13}$$

Y_F is a geometric factor, whose values are given by the following expressions:

Straight crack front

$$Y_F(a/D) = g(0.953 + 0.199(1 - \sin \psi)^4) \tag{14}$$

$$g = 0.5857(\tan \psi / \psi)^{0.5} / \cos \psi \tag{15}$$

$$\psi = (\pi a) / (4R) \tag{16}$$

Semicircular crack front

$$Y_F(a/D) = 1.04 - 3.64(a/D) + 16.86(a/D)^2 - 32.59(a/D)^3 + 28.41(a/D)^4 \tag{17}$$

Considering this solution, Fig. 12 shows the evolution of the loading conditions following the $K_r(L_r)$, being $K_r = K_I/K_{IC}$ and $L_r = P/P_L$. The intersection of the loading line $K_r(L_r)$ with the failure assessment line (FAL) defines the failure conditions, which corresponds to plastic collapse ($L_r > 1$).

The results are:

Straight crack front

Option 0: $P = 0.566$ kN

Option 1: $P = 0.582$ kN

Semicircular crack front

Option 0: $P = 0.895$ kN

Option 1: $P = 0.915$ kN

Therefore, the supported load is between 0.582 kN and 0.915 kN. The actual supported load is 0.735 kN, so it can be said that the hypothesis of a crack front between straight and semicircular and peak loads of 1.0 BW is

quite reasonable. Some conclusions can already be obtained, in good agreement with fractographic analysis and common sense:

- Critical loading conditions corresponding to a normal weight.
- Final failure due to plastic collapse of residual ligament.
- Real situation: the patient's weight is 0.735 kN, so it may be said that the crack front hypothesis in an intermediate situation between a straight crack front and a semicircular crack front is very reasonable, as are also the peak forces equal to one at the moment of fracture.

4.3.2. Fatigue

Once the failure conditions have been assessed, it is possible to perform a fatigue crack growth assessment, because there is an initial defect and the Paris law is available (Route 4 in FITNET fatigue module, [15]). Therefore, the crack growth time until critical size is reached can also be obtained. The fatigue crack growth rate is adjusted by Eq. (4).

The load cycle to which the element is subjected varies from 0, support from the other leg or repose, up to 631.5 MPa (or 252.6 MPa), corresponding to the weight of 0.735 kN and peak forces of 2.5 BW (or 1.0 BW). Thus the ΔK_I will have a value, depending on a , given by:

$$\Delta K_I = Y_F(a/D) \cdot \Delta\sigma \cdot (\pi a)^{0.5} \quad (18)$$

Taking $a_0 = 0.1$ mm as the initial crack length (after the fractographic analysis), introducing Eq. (18) in Eq. (4) and integrating this, the number of cycles required for the crack to reach the critical size of 6.5 mm is obtained. The number is between 145.738 cycles (straight front crack) and 593.088 (semicircular crack) for peak forces equal to 2.5 BW and between 6.39 (straight) and 26.5 (semicircular) millions of cycles for peak forces equal to 1.0 BW. This process can be divided in small steps and results are given in Tables 2 and 3.

According with the conditions proposed for “normal” life (2.5 BW), the cycles obtained represent between 1.3 and 4.6 months of quick propagation before failure, depending on the crack front shape. However, the propagation under these conditions finished a few thousands of cycles before, when the patient starts to feel pain and, then, a new stage starts under new loading conditions (1.0 BW). Fig. 13 shows that wherever the quick propagation finishes, it takes around 140,000 cycles in case the crack front is straight or 500,000 cycles in case the crack front is semicircular.

Considering that there is no nucleation time due to the notch effect and adding a quick propagation step of 1.3 months (equivalent to near 140.000 cycles) for a straight front crack and 4.6 months (equivalent to near 500.000 cycles) for a semicircular crack, the duration of the final stage (BW = 1.0) can be obtained. This is 7.7 months for a straight front and 4.4 months for a semicircular front. This is equivalent to 415.800 and

Table 2
Determination of the crack growth time until the critical size is reached (BW = 2.5)

a (mm)	a med (mm)	Y (straight)	Y (f.semic.)	ΔN (straight)	ΔN (semic.)	N (straight)	N (semic.)
0.1–0.5	0.30	0.945	0.660	108,999	490,750	108,999	490,750
0.5–1	0.75	0.849	0.644	18,829	59,855	127,828	550,605
1–1.5	1.25	0.792	0.635	7961	20,040	135,789	570,645
1.5–2	1.75	0.771	0.635	4294	9709	140,083	580,354
2–2.5	2.25	0.776	0.643	2449	5377	142,533	585,731
2.5–3	2.75	0.799	0.661	1420	3139	143,953	588,870
3–3.5	3.25	0.836	0.689	824	1857	144,777	590,727
3.5–4	3.75	0.889	0.728	471	1089	145,248	591,816
4–4.5	4.25	0.963	0.781	259	623	145,507	592,438
4.5–5	4.75	1.069	0.852	133	343	145,640	592,781
5–5.5	5.25	1.218	0.945	62	180	145,702	592,961
5.5–6	5.75	1.431	1.071	26	88	145,728	593,049
6–6.5	6.25	1.729	1.242	10	40	145,738	593,088
BW = 2.5						N total	

Table 3

Determination of the crack growth time until the critical size is reached (BW = 1.0)

a (mm)	a med (mm)	Y (straight)	Y (f.semic.)	ΔN (straight)	ΔN (semic.)	N (straight)	N (semic.)
0.1–0.5	0.30	0.945	0.660	5,067,464	22,815,433	5,067,464	22,815,433
0.5–1	0.75	0.849	0.644	667,745	2,122,708	5,735,208	24,938,140
1–1.5	1.25	0.792	0.635	291,380	733,428	6,026,589	25,671,568
1.5–2	1.75	0.771	0.635	158,425	358,205	6,185,014	26,029,773
2–2.5	2.25	0.776	0.643	90,659	199,035	6,275,672	26,228,808
2.5–3	2.75	0.799	0.661	52,641	116,360	6,328,313	26,345,168
3–3.5	3.25	0.836	0.689	30,590	68,903	6,358,903	26,414,071
3.5–4	3.75	0.889	0.728	17,494	40,417	6,376,397	26,454,488
4–4.5	4.25	0.963	0.781	9609	23,124	6,386,006	26,477,612
4.5–5	4.75	1.069	0.852	4930	12,740	6,390,936	26,490,352
5–5.5	5.25	1.218	0.945	2305	6673	6,393,241	26,497,025
5.5–6	5.75	1.431	1.071	970	3275	6,394,211	26,500,299
6–6.5	6.25	1.729	1.242	369	1478	6,394,580	26,501,777
BW = 1.0						N total	

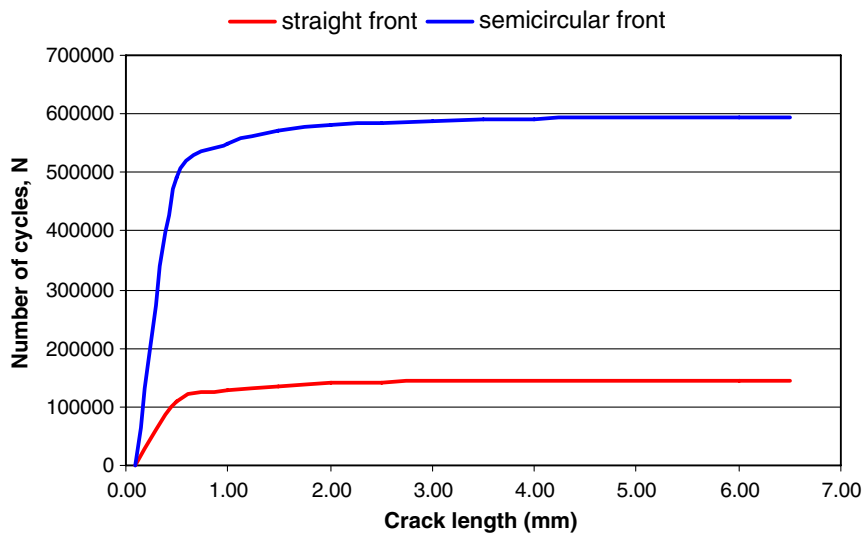


Fig. 13. Crack length evolution as a function of the number of fatigue cycles.

237.600 cycles respectively. If we start to count the cycles from the end to the beginning of the process, we obtain that such numbers are the amount of cycles that are necessary for a growth from 1.5 mm to 6.5 mm (straight) or from 2.0 mm to 6.5 mm (semicircular). As a summary, a fatigue process can be suggested as follows:

- No crack nucleation, as initial notches of 0.1 mm have been detected.
- Stage 1: Propagation with dynamic effects, from 0.1 mm to a value between 1.5 and 2.0 mm. Taking mean values, this would take about 3 months (between 1.3 and 4.6).
- Stage 2: Propagation without dynamic effects. This takes the rest of the implant life (an average of 6 months).

It is important to notice that the value taken for the peak forces have a considerable influence on the results. If the fatigue analysis is repeated with different values of the peak forces, whichever is the value taken, the crack length at which stage 2 starts remains roughly constant (between 1.5 and 2.0 mm) but the number of cycles and the time necessary to reach such stage varies sensitively, as shown in Table 4.

Table 4
Sensitivity analysis for the fatigue process considering different values of the peak forces

Peak forces	Cycles to reach stage 2 (straight)	Cycles to reach stage 2 (semicircular)	Months to reach stage 2 (straight)	Months to reach stage 2 (semicircular)	Months to reach stage 2 (average)
2.0 BW	330,000	1,400,000	3.0	12.9	7.9
2.25 BW	210,000	900,000	1.9	8.3	5.1
2.5 BW	140,000	500,000	1.3	4.6	3.0
2.75 BW	85,000	360,000	0.8	3.3	2.0
3.0 BW	60,000	250,000	0.6	2.3	1.5

From [17–22], peak forces of 2.0 BW and 3.0 BW seem to be not very realistic. Considering values from 2.25 to 2.75 BW, it can be seen that stage 2 would be reached within the second and the fifth month. If we compare it with the real case (the patient started to feel pain and use crutches during the third month), the original assumption of 2.5 BW is the most adjusted.

5. Conclusions

The main conclusion is that a reasonable solution, based on normal conditions, has been obtained in order to justify the observed failure. After the analysis performed in this paper it can be established that failure was produced by plastic collapse after a fatigue process. The irregularities found in the interphases between base material and the coatings produced a notch effect that led to a crack and its propagation.

The application of FITNET FFS procedure to this failure analysis has produced good results given that they explain the process and the incidents between the surgery operation and the failure. Also, the hypothesis of a crack whose front geometry is something between semicircular and straight as well as the hypothesis of peak forces around 2.5 BW seems to be reasonable and their results agree with the real process. Different values of the peak forces have been considered and although the quantitative results vary sensitively, the qualitative explanation of the process does not change. Also, the assumption of 1.0 BW peak forces on the quick propagation stage, proposed from the analysis of the working conditions at that stage, was validated in the fracture analysis of the implant (obtaining the exact weight of the patient) and correlates with the process observed on the patient.

From the results obtained, it can be noticed that failure occurred after a normal use of the implant, with no overloading. Therefore, if the same materials are used, a careful control on surface state to avoid or minimise imperfections in the interphases should be carried out.

References

- [1] Donachie M. Biomedical alloys. *Advanced materials & processes*, 7/98. p. 63–5.
- [2] Caron RN, Staley JT. *Materials selection and design*. ASM handbook, vol. 20. Ohio, USA: ASM International; 1997 [First printing].
- [3] Eylon D, Newman JR. *Properties and selection: nonferrous alloys and special-purpose materials*. 10th ed. Metals handbook, vol. 2. Ohio, USA: ASM International; 1990.
- [4] Buchanan JM. Experience with furlong HA.C coated implants in THR. In: *Proceedings of hydroxyapatite ceramic. A decade of experience in hip arthroplasty*, Royal College of Surgeons of England, 1995.
- [5] Kummer B. The importance of design in the stress transmission from prosthesis to bone. In: *Proceedings of hydroxyapatite ceramic. A decade of experience in hip arthroplasty*, Royal College of Surgeons of England, 1995.
- [6] Hübler R, Cozza A, Marcondes TL, Souza RB, Fiori FF. Wear and corrosion protection of 316-L femoral implants by deposition of thin films. *Surf Coat Technol* 2001;142–144:1078–83.
- [7] Mändl S, Rauschenbach B. Improving biocompatibility of medical implants with plasma immersion ion implantation. *Surf Coat Technol* 2002;156(1–3):276–83.
- [8] Wolner C, Nauer GE, Trummer J, Putz V, Tschegg S. Possible reasons for the unexpected bad biocompatibility of metal–non-metal hip implants. *Mater Sci Engng: C* 2006;26(1):34–40.
- [9] López-Sastre Nuñez A, Val Bernal J, Gonzalo Orden JM, Gorrochategui Sánchez I, Buelta Carrillo L, Lopez Sastre A. La influencia del revestimiento de hidroxiapatita y de biovidrio en la osteointegración de implantes de titanio. *Rev Ortop Traumatol* 1997;41: 173–81.

- [10] Furlong R. Osborn Supravit: El recubrimiento H-A.C. avanzado de J.R.I. Joint Replacement Instrumentation Ltd, 104–112 Marylebone Lane, London W1M 5FU.
- [11] Semlitsch MF, Panic B, Weber H, Schoen R. Comparison of the fatigue strength of femoral prosthesis stems made of forged Ti–Al–V and cobalt-base alloys. STP 796. Philadelphia: ASTM; 1983.
- [12] Semlitsch MF, Panic B. Corrosion fatigue testing of femoral head prostheses made of implant alloys of different fatigue resistance. In: Winter GD et al., editors. Evaluation of biomaterials. John Wiley & Sons; 1980.
- [13] Lin CW, Ju CP, Chern Lin JH. A comparison of the fatigue behaviour of cast Ti–7.5Mo with c.p titanium, Ti–6Al–4V and Ti–13Nb–13Zr alloys. *Biomaterials* 2005;26(16):2899–907.
- [14] Filip R, Kubick K, Ziaja W, Sieniawski J. The effect of microstructure on the mechanical properties of two-phase titanium alloys. *J Mater Process Technol* 2003;133(1–2):84–9.
- [15] FITNET, European Fitness-for-Service (FFS) Network. GIRT-CT-2001-05071. Available from: <http://www.eurofitnet.org>.
- [16] SINTAP, Structural INTEgrity Assessment Procedure, Final Revision. EU-Project BE 95-1462. Brite Euram Programme, 1999.
- [17] Van der Bogert AJ, Read L, Nigg BM. An analysis of hip joint loading during walking, running and skiing. *Med Sci Sports Exerc* 1999;31:131–42.
- [18] Taylor SJ, Walker PS. Forces and moments telemetered from two distal femoral replacements during various activities. *J Biomech* 2001;34(July):839–48.
- [19] Taylor SJ, Walker PS, Perry JS, Cannon SR, Woledge R. The forces in the distal femur and the knee during walking and other activities measured by telemetry. *J Arthroplasty* 1998;13:428–37.
- [20] Kotzer GM, Davy DT, Goldberg VM, Heipke KG, Berilla J, Heipke Jr KG, et al. Telemeterized in vivo hip joint force data: a report on two patients after total hip surgery. *J Orthop Res* 1991;9(5):621–33.
- [21] Brand RA, Pedersen DR, Davy T, Kotzar GM, Heipke KG, Goldberg VM. Comparison of hip force calculations and measurements in the same patient. *J Arthroplasty* 1994;9(1):45–51.
- [22] Stansfield BW, Nicol AC. Hip joint contact forces in normal subjects and subjects with total hip prostheses: walking and stair and ramp negotiation. *Clin Biomech (Bristol, Avon)* 2002;17(2):130–9.
- [23] Bergmann B, Deuretzbacher G, Heller M, Graichen F, Rohlmann A, Strauss J, et al. Hip contact forces and gait patterns from routine activities. *J Biomech* 2001;34:859–71.
- [24] Heller MO, Bergmann G, Deuretzbacher G, Dürselen L, Pohl M, Claes L, et al. Musculo-skeletal loading conditions at the hip during walking and stair climbing. *J Biomech* 2001;34:883–93.
- [25] Heller MO, Bergmann G, Deuretzbacher G, Claes L, Haas NP, Duda GN. Influence of femoral anteversion on proximal femoral loading: measurement and simulation in four patients. *Clin Biomech* 2001;16:644–9.
- [26] Metals handbook, vol. 2 – Properties and selection: nonferrous alloys and special-purpose materials. 10th ed. ASM International; 1990.